*Communications in Computational Chemistry*
*Commun. Comput. Chem., Vol. 1 , No. 1* , 1–12
doi: 10.4208/cicc.2024.334.01

**Regular Article**

# Therapeutic Potential and Mechanistic Insights of Sunflower Receptacles' Essential Oil Against Gout: An In-Depth Molecular Study

**Kaiyu Wang†, Xue Bai†, Hengzheng Yang, Kaifeng Liu, Lu Han, Wannan Li* and Weiwei Han***

School of Chemistry and Chemical Engineering, Shandong University, Jinan, 250010, People's Republic of China

*Corresponding author: liwannan@jlu.edu.cn; weiweihan@jlu.edu.cn (W.H.)

Received on 29 November 2024; Accepted on 12 February 2025

## Abstract

Gout is a common chronic disease caused by the deposition of monosodium urate crystals. Previous studies confirmed the anti-gout effects of sunflower receptacles. For example, eupatoriochromene may be one of the most important compounds for reducing uric acid and relieving gout, which can be extracted from the essential oil of sunflower receptacles (EOSR). However, the other active components in EOSR and their anti-gout molecular mechanisms remain unclear. In this work, we employed widespread methods such as network pharmacology, machine learning algorithm, molecular docking, and molecular dynamics simulation, to investigate the anti-gout molecular mechanisms of the EOSR components. The protein- protein interaction (PPI) network confirmed that the components of EOSR exert anti-gout effects mainly by targeting inflammatory targets. GO and KEGG enrichment analyses revealed that the components of EOSR play roles in several important biological pathways, potentially providing anti-gout effects through various mechanisms. Additionally, since the target URAT1 plays a critical role in the treatment of gout, we investigated the interactions between two components of EOSR, Linoleic acid (La) and Kauren-19-oic acid (Koa), and target URAT1 using machine learning algorithm, molecular docking and molecular dynamics simulation. It confirmed that La and Koa can stably bind to URAT1 and shift its conformation to the Inward-facing state. Similar to the positive control Benzbromarone (Ben), both La and Koa induce secondary structural changes in URAT1, with Koa sharing key residues with Ben. This research further indicates the molecular mechanisms of EOSR in treating gout and expands the range of therapeutic agents for it.

**Key words:** Essential oil of sunflower receptacles, gout, molecular dynamics simulation, Markov state model.

## 1. Introduction

Gout is an inflammatory disease that causes significant pain and discomfort for patients [1,2]. In the United States, approximately 12 million adults have experienced gout [3]. It is primarily caused by elevated serum uric acid levels, which lead to the deposition of excess urate crystals in joints, soft tissues, and other organs, causing inflammation and severe pain [4,5]. Current treatments for gout include drugs to relieve acute gout attacks. Medications such as etoricoxib and colchicine help reduce joint redness, swelling, and pain by inhibiting inflammation [6,7]. And for long-term management, drugs that control serum uric acid levels are used. This is primarily achieved through two mechanisms: inhibiting uric acid production and promoting uric acid excretion [8–11]. For example, allopurinol reduces uric acid production by inhibiting the key enzyme xanthine oxidase (XO), while benzbromarone reduces uric acid reabsorption in the renal tubules by inhibiting the urate transporter protein (URAT1) and other related transporters. XO and URAT1 are widely recognized in the academic literature and clinical practice as critical targets for gout treatment [12–14].

Kaiyu Wang and Xue Bai contributed equally



 

However, previous medications can cause side effects such as liver and kidney damage and increase the risk of cardiovascular events [15]. Th erefore, research into new therapies for gout is crucial and of great importance.

As a member of the Asteraceae family, sunflower (Helianthus annuus L.) is one of the traditional crops in China, primarily cultivated for its edible seeds. In addition, the receptacles of the sunflower are rich in chemical components with anti-inflammatory, antioxidant, and hepatoprotective properties, which is of great research significance [16–18]. Converting sunflower receptacles into essential oil helps preserve their active compounds and extend their shelf life. According to our preliminary research, the components of sunflower receptacles exhibit promising anti-gout effects [19]. For example, eupatoriochromene, a compound in sunflower receptacle essential oil (EOSR), significantly reduces uric acid levels [20]. However, other active compounds in EOSR and their specific anti-gout mechanisms have yet to be thoroughly studied.

Considering the significant role of natural plant components in disease treatment and the widespread application of network pharmacology, machine learning, molecular docking, and molecular dynamics (MD) simulations, we employed these methods to study the anti-gout mechanisms of EOSR components [21–23]. We used network pharmacology to analyze the comprehensive mechanisms of EOSR components within biological systems. Then, machine learning algorithms and molecular docking were used to indicate the interactions between proteins and small molecules. Furthermore, MD simulations was used to offer dynamic modeling and reveal conformation transitions. This research not only revealed the bioactive components in EOSR and their anti-gout mechanisms but also provided theoretical foundations and references for developing new anti-gout drugs. These findings will help enhance current gout treatments, improve their effectiveness, and support the rational use of traditional medicinal resources.

## 2. Theoretical method

### 2.1 Identification of gout-related targets

We screened for gout target genes from DisGeNET (https://www.disgenet.org/) [24], GeneCards (https://www.genecards.org/) [25], and PharmGKB (https://www.pharmgkb.org/) [26]. We identified 196 potential targets in DisGeNET databases, 928 potential targets in GeneCards and 7 potential targets in PharmGKB. After performing a union operation on the potential targets from three databases, 996 unique potential targets were obtained.

### 2.2 Prediction of targets of EOSR components

We screened SwissTargetPrediction (http://swisstargetprediction.ch/) [27] for potential targets of EOSR components. We identified 551 potential targets in the 104 components.

### 2.3 Identification of common targets of gout and EOSR components and construction of the PPI Network

We utilized the online tool jvenn (https://jvenn.toulouse.inra.fr/app/example.html) [28] to assess the overlap of targets of gout and EOSR components. The construction of the PPI network relied on data sourced from the STRING database (http://string-db.org/) [29] to evaluate potential interactions among the identified targets. We used Cytoscape 3.9.1 [30] to visually represent these interactions. Subsequently, using the cyto-Hubba plugin, we analyzed the topological properties of the network through the MCC method and identified the top 15 ranked targets.

### 2.4 GO and KEGG enrichment analysis

We employed several R packages-clusterProfiler, AnnotationHub, org.Hs.eg, enrichplot, pathview, dplyr, and ggplot2-for conducting enrichment analyses on GO biological processes and KEGG based on common targets of gout and EOSR components. Utilizing a significance threshold of $p = 0.01$ and $q = 0.01$, we retrieved GO information from org.Hs.eg.Db and KEGG information from clusterProfiler. The outcomes were presented through bar charts and bubble charts to offer a comprehensive visualization of the final results.

### 2.5 Molecular docking and machine learning algorithms

Due to the lack of a resolved crystal structure for URAT1, we utilized the URAT1 structure constructed by AlphaFold2. Additionally, the small molecule structures of Ben, La, and Koa were obtained from PubChem. The Flexible Docking module in Discovery Studio 2019 was used for the docking process. For selecting the docking site of URAT1, although its crystal structure has not yet been resolved, several studies have identified key residues. Yanyu Chen et al. verified that mutating the Ser35 and Phe241 residues to alanine significantly impairs the urate transport function of URAT1, providing a theoretical basis for the docking of URAT1 [31]. Based on the report, we selected Ser35 and Phe241 as the approximate positions for the docking box. The results of molecular docking were visualized using PyMOL 2.5.7 [32] and Discovery Studio 2019. Additionally, in this study, we applied the machine learning algorithm ConPLex [33], which integrates pretrained protein language models (PLMs) with contrastive learning techniques [34]. ConPLex predicted the binding potential of the components to the target protein based on their chemical structure, which were represented as SMILES strings.

### 2.6 Construction of membrane protein system using Charmm-GUI

Using Charmm-GUI (https://www.charmm-gui.org/?doc=input/membrane.bilayer), we constructed the membrane protein system for URAT1. In the Orientation Options, we selected PPM2.0 [35] to determine the position of the phospholipid bilayer relative to the protein. We set the water thickness to 15 Å (the minimum distance between the protein and the edge is 15 Å), the lipid type to POPC, and the lengths of X and Y to 110 Å, with NaCl as the equilibrating ion. Other settings were kept as default. For the Force Field Options, we selected the AMBER force field: FF14SB [36] for the protein, Lipid21 for the phospholipids, TIP3P [37] for water, and GAFF2 [38] for the small molecules [39].

### 2.7 Molecular dynamics simulations

Using AMBER 16's PMEMD engine, we conducted MD simulations on our systems, employing periodic boundary conditions to prevent edge effects. Based on the mdin files provided by Charmm-GUI, we conducted steps involving energy minimization, equilibration and production.

During the energy minimization phase, a total of 5000 steps were performed. The first 2500 steps were carried out using the steepest descent method, while the remaining steps used the conjugate gradient method. A nonbonded interaction cutoff of 9.0 Å was applied, and positional restraints were applied to the protein and membrane systems to maintain their stability.

According to the parameters set by CHARMM-GUI, the equilibration phase consisted of six steps. The first two steps were NVT simulations, during which the system was gradually heated to 303.15 K and maintained at this temperature. The next four steps were NPT simulations, in which the system was further equilibrated at a constant temperature of 303.15 K and pressure of 1.0 bar. In the first three stages, a time step of 0.001 ps was used for 125 ps of equilibration. And in the next three stages, the time step was increased to 0.002 ps, with each stage lasting 500 ps. Throughout the equilibration process, positional restraints on the protein and membrane were gradually reduced from initial values of 10 kcal/mol/Å$^2$ and 2.5 kcal/mol/Å$^2$ to a fully unrestrained state.

During the production phase, a total of 500 ns was simulated under NPT conditions with a time step of 0.004 ps. The pressure was maintained using the Berendsen barostat with semiisotropic pressure scaling, where the pressure in the x/y directions (parallel to the interface) and the z-direction were both set to 1 bar, with a pressure coupling time constant of 1 ps. The temperature was controlled using the Langevin thermostat at 303.15 K with a collision frequency $\gamma$ of 1 ps$^{-1}$ [40].

The MD analyses were conducted using CPPTRAJ [41]. Due to the high flexibility of the C-terminal structure of URAT1 (residues 521-553) and its lack of interaction with small molecule compounds, substrates, or other parts of the protein, the tail region of the protein was not considered in the analysis. Only residues 1-520 were analyzed.

Similar to our previous work [22], we employed the molecular mechanics/Poisson–Boltzmann surface area (MM/PBSA) method to investigate the binding affinity between the compounds and URAT1. The binding free energy is described by ($\Delta G_{\mathrm{bind}}$) the following equation:

$$\Delta G_{\mathrm{bind}} = \Delta H - T\Delta S, \tag{1}$$

$$\Delta H = \Delta E_{\mathrm{MM}} + \Delta G_{\mathrm{sol}}, \tag{2}$$

$$\Delta E_{\mathrm{MM}} = \Delta E_{\mathrm{ele}} + \Delta E_{\mathrm{vdW}} + \Delta E_{\mathrm{int}}, \tag{3}$$

$$\Delta G_{\mathrm{sol}} = \Delta G_{\mathrm{pb}} + \Delta G_{\mathrm{np}}. \tag{4}$$

In these equations, $\Delta E_{\mathrm{MM}}$ refers to the gas-phase energy, $\Delta G_{\mathrm{sol}}$ to the solvation free energy, $\Delta E_{\mathrm{ele}}$ to the electrostatic energy, $\Delta E_{\mathrm{vdW}}$ to the van der Waals energy, $\Delta E_{\mathrm{int}}$ to the internal energy, $\Delta G_{\mathrm{pb}}$ to the polar solvation energy, and $\Delta G_{\mathrm{np}}$ to the non-polar solvation energy.

In our 500 ns MD simulation, MM/PBSA calculations were performed on one frame every 5 ns, and the binding free energy was averaged over 100 frames. The calculations used default atomic radii and an ionic strength of 0.15 mol/L. The decomposition of van der Waals, electrostatic, and solvation energies was carried out at the residue level to identify key binding residues. Other parameters were set to their default values.

### 2.8 PCA analysis and Caver analysis

Using CPPTRAJ, the trajectory was projected onto the first two principal components, and the results were analyzed and plotted using the converting dot distribution to probability distribution (ddtpd) program. The minimum free energy corresponding structure was analyzed using the CAVER 3.0.3 PyMOL Plugin. Ser35, Phe241, Phe365, and Phe449 were selected as reference coordinates for the channel starting point. For the Ben, La, and Koa systems, the Minimum Probe Radius was set to 1.5 and the Shell Radius to 6. Due to the large setting of Minimum Probe Radius and Shell Radius, which resulted in no available channels, the default values (Minimum Probe Radius of 0.9 and Shell Radius of 3) were used for the Apo system. All other settings were kept as default.

### 2.9 DSSP analysis

RMSF and DSSP data were calculated using CPPTRAJ. The results were then visualized using Gnuplot 6.0.

### 2.10 Key residue analysis

The contribution of each residue to the binding free energy in each system was analyzed using MM-PBSA. The top 10 residues were then plotted. The hydrogen bond analysis was conducted using CPPTRAJ. Representative conformations were obtained through K-means clustering and PCA analysis.

### 2.11 Markov state models analysis

Following the methods outlined in the Amber tutorials, we performed a Markov model analysis. Using the PyEMMA 2.5.7 [42] package, we analyzed the 500 ns trajectory data for each system. To avoid noise and reduce computational costs, we estimated the channel size and used it as a feature using the MDAnalysis 2.2.0 [43] package. Additionally, the minimum RMSD was also used as a feature. The trajectory feature matrix was constructed based on the selected features, followed by dimension reduction using TICA (Time-lagged Independent Component Analysis) and K-means clustering. Subsequently, an appropriate lag time was selected. From Figure S5, we observed that at a lag time of 2, the implied timescales (ITS) stabilized with increasing lag time, indicating that the system had converged to a steady state and was no longer sensitive to further lag time increases. Such convergence confirmed that the current state contained sufficient information to predict future behavior, demonstrating true Markovian dynamics. Figure S6 shows the identification of major conformational transitions through ITS, which help determine the system's main global states. We test the validity of the estimated Markov State Models (MSM) using the Chapman-Kolmogorov test. Simply put, this test compares a quantity at lag time k$\tau$ predicted by the MSM at lag time $\tau$, with a MSM estimated directly at k$\tau$. As shown in Figure S7, the predicted curves and the estimate curves align closely, indicating that the system's dynamics are Markovian, and the models are valid.

## 3. Results and discussion

Figure 1 illustrates the specific workflow of our study. First, we identified gout-related targets and predicted the targets of EOSR components using various databases. For the common targets, we conducted a PPI network analysis and reviewed the relevant literature to determine potential direct targets of EOSR for gout

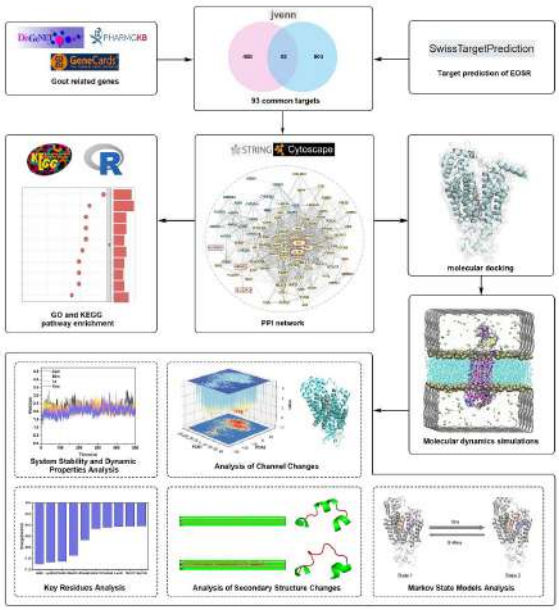


**Figure 1.** Workflow illustrating the integration of network pharmacology, molecular docking, and molecular dynamics (MD) simulations to investigate the anti-gout mechanisms of the essential oil of sunflower receptacles (EOSR). The process includes the identification of potential targets through network pharmacology, binding affinity assessment via molecular docking, and the evaluation of the stability and dynamics of the interactions using MD simulation.

intervention, ultimately selecting URAT1 for further analysis. Additionally, we performed GO and KEGG pathway enrichment analyses to map individual targets to relevant pathways, thus assessing the overall mechanisms by which EOSR might affect gout. Following this, we conducted molecular docking and MD simulations of URAT1 with two EOSR components. We analyzed the MD trajectories using five different methods to evaluate the specific binding mechanism of the small molecules with URAT1 and the resulting conformational changes.

### 3.1 Identification of common targets between EOSR components and gout

Using the DisGeNET, GeneCards, and PharmGKB databases, we identified 903 targets associated with gout. Based on our previous research [20], we characterized 104 compounds in the EOSR (see Table S1). Target prediction for these compounds by the SwissTargetPrediction (STP) database revealed 551 targets with a probability $> 0$. Among these, there are 93 common targets between gout and EOSR (see Figure S1 and Table S2). These targets are potential targets for EOSR components to intervene in gout.

### 3.2 PPI network analysis on common targets in gout and EOSR

The 93 common targets between gout and EOSR were input into the STRING database to construct a protein-protein interaction (PPI) network. The PPI network was visualized using Cytoscape, as shown in Figure 2A. Using k-means clustering, the targets were grouped into five clusters, with targets in the same cluster showing closer interactions than those in different clusters. Detailed network information is provided in Table 1. Additionally, the CytoHubba plugin was employed to perform a topological analysis of the network using the Maximal Clique Centrality (MCC) method. The top 15 key targets and their relationships are shown in Figure 2C. Notably, inflammatory factors such as IL6 and TNF scored highly and ranked among the top. EOSR showed potential for relieving acute gout attacks through its anti-inflammatory properties. To further identify the key targets, we reviewed the relevant literature and marked the most directly gout-associated targets using red boxes in Figure 2A. Detailed information about these targets is provided in Table 2 and the relationships among these targets are illustrated in Figure 2B. Based on the results, we propose that EOSR not only exerts anti-inflammatory effects by targeting inflammatory factors such as IL6, IL1B, and TNF, but also influences uric acid excretion and reabsorption by targeting genes like ABCG2, SLC22A12, and SLC22A6. Among these, SLC22A12 encodes URAT1, a key target of the gout drug benzbromarone. Inhibiting URAT1 has been shown to be an effective treatment for gout [12–14]. Therefore, URAT1 was selected for our further docking studies.

**Table 1.** PPI network stats.

| Property | Value |
|---|---|
| number of nodes | 93 |
| number of edges | 949 |
| average node degree | 20.4 |
| avg. local clustering coefficient | 0.64 |
| expected number of edges | 380 |
| PPI enrichment p-value | $< 1.0e-16$ |

### 3.3 GO and KEGG enrichment analysis

Gene Ontology (GO) enrichment analysis is a popular method for evaluating the enrichment of GO terms within a set of genes [48]. It typically categorizes genes into three main levels: Cellular Component (CC), Biological Process (BP), and Molecular Function (MF). The Kyoto Encyclopedia of Genes and Genomes (KEGG) pathway enrichment analysis focuses on describing the roles of genes within metabolic and signaling pathways. By examining the enrichment of pathways within the genome, we can gain a comprehensive understanding of the functions and regulatory mechanisms of these genes in the organism.

Enrichment analysis of GO and KEGG pathways was performed using the 93 common targets between gout and EOSR. As shown in Figure 3, the calculated data was demonstrated as a bubble chart and bar plot.

In the potential Biological Processes (BP) associated with the common targets, components of EOSR exhibit responses to xenobiotic stimulus, nutrient levels, steroid hormones, lipopolysaccharide, molecules of bacterial origin, chemical stress, and oxidative stress, which suggests that these components can modulate responses to a diverse range of stressors and toxins. Additionally, they play roles in the regulation of protein secretion and the inflammatory response, highlighting their potential usefulness in managing inflammation and infections. Furthermore,

**Table 2.** Direct targets of EOSR intervention in gout.

| Target | Description |
|---|---|
| **SLC22A6** | encoding the urate reabsorption transporter OAT1 [44] |
| **ABCG2** | Responsible for a significant portion of extra-renal urate excretion [45] |
| **SLC22A12** | Encoding the URAT1 protein, the primary protein for renal tubular reabsorption of urate [5] |
| **IL6 and TNF** | Pro-inflammatory mediators and markers of gouty arthritis [46] |
| **IL-1$\beta$** | A critical pro-inflammatory cytokine in acute gouty arthritis, which initiates the production and secretion of other inflammatory mediators like IL-6 and IL-8 [47] |

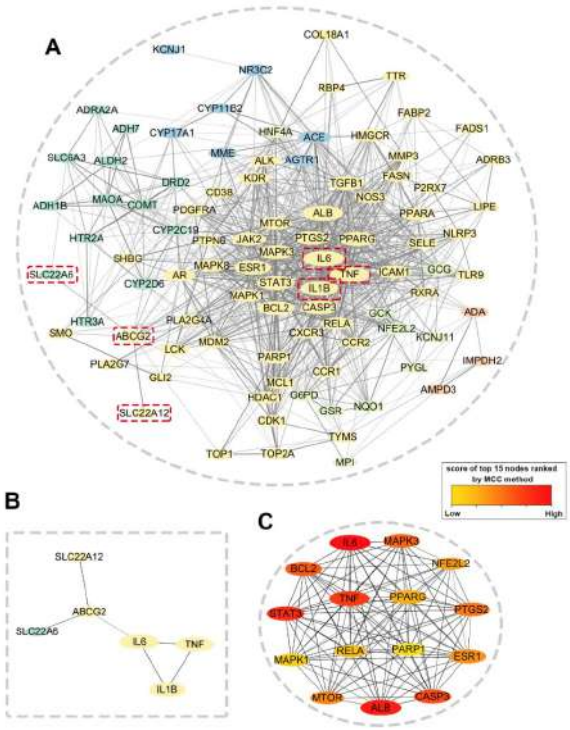


**Figure 2.** (A) Protein-protein interaction (PPI) network of common targets. Different groups represented by different colors. (B) PPI network of targets most directly related to gout. (C) PPI network of the top 15 key targets.

the discovery of rhythmic processes indicates their involvement in adjusting biological rhythms.

The enriched Cellular Components (CC) identified for the common targets indicate that EOSR are most likely to act on cell membranes. Their action is associated with membrane-related sites such as membrane rafts, membrane microdomains, the external side of the plasma membrane, caveolae, and plasma membrane rafts. Additionally, lumens are also potential targets, including the cytoplasmic vesicle lumen, vesicle lumen, and secretory granule lumen. Furthermore, two unique results appear in the top ten cellular components: the neuronal cell body and the dopaminergic synapse, which are potential sites of action for EOSR.

The molecular function (MF) analysis of the common targets of EOSR and gout reveals that these natural components may regulate gout through multiple mechanisms. Firstly, they may participate in the regulation of gene transcription by interacting with DNA-binding transcription factors and RNA polymerase II-specific DNA-binding transcription factors, thereby influencing transcriptional activity. The involvement in transcription coregulator binding suggests that these compounds may interact with coregulators during transcription, further modulating gene expression. Moreover, the enrichment in nuclear receptor activity and ligand-activated transcription factor activity indicates that these natural products may influence nuclear receptor-related signaling pathways, affecting cellular biological responses. The enrichment in phosphatase binding suggests they might regulate phosphorylation processes, while catecholamine binding indicates potential effects on neurotransmitter activity. Finally, the findings of carboxylic acid binding, organic acid binding, and monocarboxylic acid binding suggest that these natural components may play roles in metabolic processes.

As illustrated in Figure 3B, the KEGG enrichment analysis of EOSR components reveals their involvement in several key biological pathways.

Firstly, the enrichment results highlight the potential of EOSR components to intervene in metabolism and cardiovascular diseases. Relevant pathways include the AGE-RAGE signaling pathway in diabetic complications, Lipid and atherosclerosis, and Fluid shear stress and atherosclerosis. This suggests that components of EOSR may reduce uric acid production in gout patients by regulating lipid metabolism, decreasing oxidative stress, and mitigating inflammatory responses, thereby alleviating gout symptoms.

Additionally, these components are involved in multiple immune and inflammatory pathways, such as Th17 cell differentiation, TNF signaling pathway, and C-type lectin receptor signaling pathway. EOSR might alleviate inflammation and pain associated with gout by inhibiting Th17 cell differentiation and some inflammatory signaling pathways, thus reducing the release of inflammatory mediators.

The analysis also uncovers the potential roles of these components in various infectious diseases (such as Human cytomegalovirus infection, Kaposi sarcoma-associated herpesvirus infection, and Leishmaniasis) and other physiological processes (such as the Prolactin signaling pathway). The antimicrobial and antiviral properties of EOSR may help mitigate gout symptoms by reducing infections and inflammation.

**Table 3.** Information on EOSR components and benzbromarone and their binding free energies with URAT1.

| Name | CAS | PubChem CID | SMILES | Total binding energy (kcal/mol) | ConPLex predict |
|---|---|---|---|---|---|
| **Linolic acid (La)** | 60-33-3 | 5280450 | CCCCCC=CCC=CCCCCCCCC(=O)O | -115.82 | 0.171 |
| **Kauren-19-oic acid (Koa)** | 6730-83-2 | 73062 | CC12CCCC(C1CCC34C2CCC(C3)C(=C)C4)(C)C(=O)O | -54.82 | 0.031 |
| **Benzbromarone (Ben)** | 3562-84-3 | 2333 | CCC1=C(C2=CC=CC=C2O1)C(=O)C3=CC(=C(C(=C3)Br)O)Br | -103.07 | 0.107 |

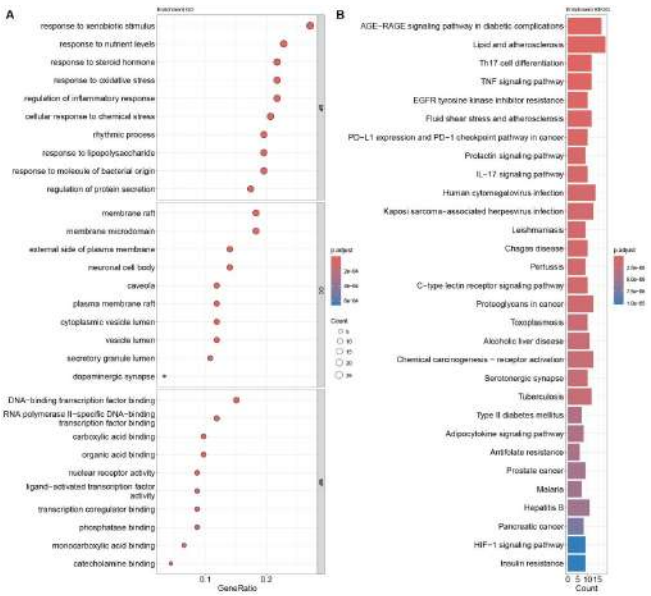


**Figure 3.** (A) Results of GO pathway enrichment analysis. GeneRatio represents the proportion of genes associated with each GO term. The circle size indicates the gene count, and the color reflects the adjusted p-value (p.adjust), with red indicating higher significance. (B) Results of KEGG pathway enrichment analysis. The bar length represents the gene count, and the color reflects the adjusted p-value, with red indicating higher significance.

### 3.4 Molecular docking and machine learning algorithms of EOSR components

To further explore the key components of EOSR and their mechanisms of influencing uric acid reabsorption, we focused on the SLC22A12 gene, which encodes the URAT1 protein. Among the 104 components of EOSR, two were predicted by STP to target SLC22A12: Linoleic acid (La) and Kauren-19-oic acid (Koa). We then performed molecular docking and applied machine learning algorithms (ConPLex) to these two components, as well as to the positive control, benzbromarone (Ben), with the target protein URAT1.

Figure 4 illustrates the binding positions and modes of the compounds. La formed conventional hydrogen bonds with the Lys393 residue and established van der Waals interactions with surrounding residues. Koa formed conventional hydrogen bonds with Ser35 and engaged in Pi-Alkyl interactions with Cys32, Met36, His245, Phe364, Phe365, and Phe449. Ben formed a halogen bond with Gln473, Pi-Pi interactions with Phe241, Phe364, and Phe449, as well as other pi interactions with Leu31, Cys32, Met214, Phe241, Phe360, and Ala476. Table 3 presents the information, docking energies, and ConPLex prediction results of the compounds. The results from both molecular docking and ConPLex showed a consistent trend, with La demonstrating better total binding energy and predicted scores. Additionally, literature suggests that La inhibits URAT1 in vitro, although its exact inhibitory mechanism remains unclear [49]. In contrast, Koa showed relatively poorer binding energy and predicted scores. However, molecular docking revealed that Koa forms a hydrogen bond with the key residue Ser35 [31], and its interacting residues significantly overlap with those of Ben. This suggests that Koa may bind to URAT1 in a similar way to Ben, making it a potential alternative to Ben as a uric acid reabsorption inhibitor. Based on these findings, we performed further molecular dynamics simulations of La and Koa with URAT1 to investigate their specific inhibitory mechanisms.

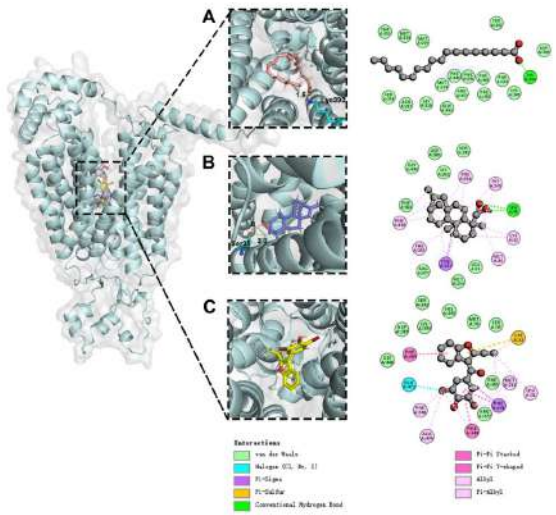


**Figure 4.** Molecular docking indicated the possible binding sites and key residues between URAT1 and (A) La, (B) Koa, and (C) Ben.

### 3.5 Molecular dynamics simulation system

To further observe the dynamic behavior and structural changes of URAT1 upon binding with compounds, we performed 500 ns MD simulations on the La-URAT1 and Koa-URAT1 complexes.

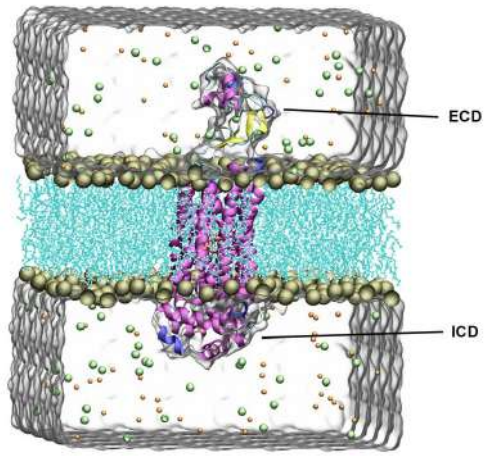


**Figure 5.** MD simulation system setup: yellow spheres represent the phospholipid bilayer headgroups, blue chains represent the tails; green spheres represent $Cl^-$ ions, and orange spheres represent $Na^+$ ions. The intracellular domain (ICD) and extracellular domain (ECD) are indicated in the figure.

Since URAT1 is a transmembrane channel protein, we employed Charmm-GUI to incorporate phospholipids of the cell membrane for a more accurate simulation of URAT1's dynamic behavior. $Na^+$ and $Cl^-$ ions were used to equilibrate the system in water boxes on both sides of the phospholipid bilayer membrane. The system setup is illustrated in Figure 5. Additionally, the simulations included the apo form of URAT1 (Apo) and the Ben-URAT1 complex as controls.

### 3.6 System stability and dynamic properties analysis

To evaluate the stability of the systems, we performed the root mean square deviation (RMSD) analysis, as shown in Figure 6A. During the first 0-100 ns, the RMSD of all four systems increased; after 100 ns, the RMSD fluctuated within approximately 1 Å, indicating that the systems had reached equilibrium and were suitable for subsequent analysis. The solvent-accessible surface area (SASA) analysis indicated the contact area between the protein and the aqueous solution; the larger the contact area, the more relaxed the protein structure. As shown in Figure 6B, the SASA fluctuations of the four systems were similar, ranging approximately between 240 and 264 $nm^2$. Further radius of gyration (Rg) analysis reflects the compactness of the protein structure, representing the degree of chain looseness during the simulation. As shown in Figure 6C, the Ben system exhibited the largest Rg, while the Apo system showed the smallest Rg. The Rg values of the La and Koa systems fell between those of the Apo and Ben systems, with this trend being particularly noticeable during the 250-500 ns interval. This indicates that benzbromarone binding loosens the URAT1 structure, while the components La and Koa from EOSR also contribute to a slight loosening of URAT1, similar to the effect of benzbromarone.

Using MM-PBSA analysis, we obtained the binding free energies of the compounds with the protein, as shown in Table 4. The binding free energies of La and Koa were lower than

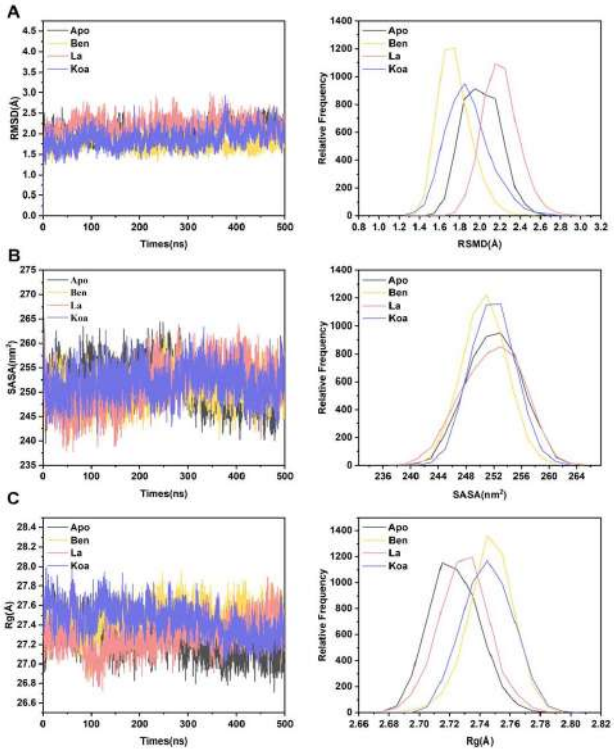


**Figure 6.** MD simulation analysis of EOSR components and Ben binding to URAT1. (A) RMSD. (B) SASA. (C) Rg.

that of Ben, with values of -31.50 ± 0.95 kcal/mol and -26.16 ± 0.94 kcal/mol. Compared to Ben, La and Koa may form a more stable complex with URAT1. The time-dependent variation of binding free energies for all three compounds with URAT1 can be seen in Figure S2. Notably, Koa's performance in the MM-PBSA analysis is better than its total binding energy observed in molecular docking. This discrepancy may be attributed to the compact structure of Koa, which results in an excessively high intramolecular energy, consequently leading to a higher total binding energy in the docking. In contrast, during MM-PBSA analysis, MD simulations allow Koa to interact with both the protein and the solvent environment, enabling it to stabilize in a lower-energy conformation, leading to a more favorable performance in MM-PBSA.

### 3.7 Analysis of channel changes during simulation

According to the cryo-EM study by Tongyi Dou et al. on the rat OAT1 (also known as SLC22A6) from the SLC22 family, OAT1 exhibits three states: Inward-facing, Occluded, and Outward-facing. When the channel is Inward-facing, the central channel is open to the intracellular side, while the N-terminal and C-terminal domains near the extracellular side form a "thick gate", preventing substrates or inhibitors from entering or exiting through extracellular domain (ECD) [50]. We hypothesize that URAT1 (SLC22A12), a member of the same family, undergoes similar structural changes.

**Table 4.** MM-PBSA analysis of Ben, La, and Koa systems. Data are presented as mean value ± standard error of the mean (SEM). All units are reported in kcal/mol.

| | **Ben** | **La** | **Koa** |
|---|---|---|---|
| $\Delta E_{\mathrm{vdW}}$ | -39.12 ± 0.28 | -39.72 ± 0.62 | -35.80 ± 0.39 |
| $\Delta E_{\mathrm{ele}}$ | -9.74 ± 0.51 | -175.61 ± 2.95 | -154.68 ± 3.88 |
| $\Delta G_{\mathrm{gas}}$ | -48.87 ± 0.54 | -215.34 ± 2.81 | -190.47 ± 3.91 |
| $\Delta G_{\mathrm{solv}}$ | 31.01 ± 0.60 | 183.84 ± 2.10 | 164.31 ± 3.32 |
| $\Delta G_{\mathrm{total}}$ | -17.86 ± 0.51 | -31.50 ± 0.95 | -26.1 ± 0.94 |

To evaluate the changes in the channel during MD simulations, we performed principal component analysis (PCA) and constructed free energy landscape diagrams to identify the structures corresponding to the minimum energy in each system. In each system, we observed one or two minimum energy states, as shown in Figure 7. We then analyzed the intracellular-facing channel using the Caver 3.0.3 PyMOL Plugin [51], and the results are summarized in Figure 7 and Table 5. The data reveal that, compared to the Apo system, the intracellular-facing channels of URAT1 when bound with compounds became wider. Specifically, the Koa and La systems demonstrated a significant increase in the average bottleneck radius, while the average tunnel throughput also exhibited an increase. The Ben system also showed moderate increases in these metrics. These changes suggest that the binding of compounds to URAT1 results in alterations to the channel dimensions, potentially influencing its functional state. Additionally, as shown in Figure 8, the channel analysis of State 2 in the Apo system revealed an extracellular-facing channel, indicating that URAT1 was approaching the Occluded state at that moment.

Overall, the binding of the compounds stabilizes URAT1 in the Inward-facing state, potentially inhibiting the process of URAT1 opening to the extracellular side and transporting urate ions. Interestingly, Shen et al. observed a similar inward-facing conformation in the binding of the compound apigenin to another urate transporter, GLUT9 [52]. We believe this could be the mechanism by which benzbromarone and the components of EOSR intervene in gout.

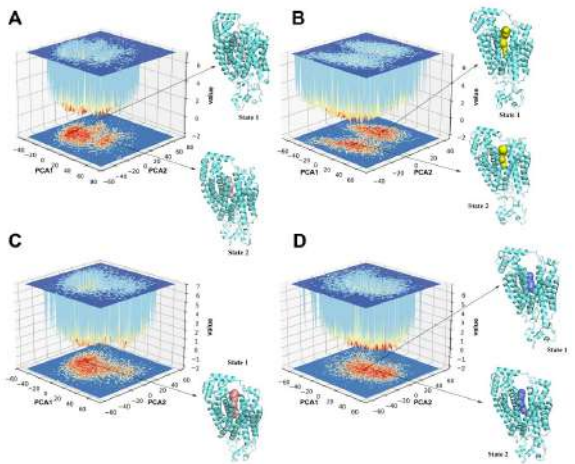


**Figure 7.** Analysis of PCA and the lowest energy conformation of the intracellular-facing channel in the four systems. PCA1 and PCA2 represent the first two principal components. The value represents the relative free energy. (A) Apo. (B) Ben. (C) La. (D) Koa.

### 3.8 Analysis of secondary structure changes during simulation

To further investigate the structural changes of URAT1 during the simulation, we conducted a detailed dictionary of secondary structure of proteins (DSSP) analysis on the four systems. The analysis results are shown in Figure S3. Based on RMSF, we further analyzed the regions with significant differences between the Apo system and the other systems. The results are presented in Figure 9.

Between residues 270-320, the Ben and Koa systems exhibit a higher probability of forming a Bend structure compared to the Apo system. In the representative conformations, the Alpha helix from residues 309-314 completely disappears in the Ben system, while it shortens in the Koa system. There is no significant difference in the secondary structure between the La and Apo systems for residues 309-314. In URAT1, residues 300-320 are located on the intracellular domain (ICD). Upon compound binding, the transition from an Alpha helix to a Bend structure makes the conformation more flexible. This finding is consistent with the Caver analysis, where the URAT1 structure bound to the compounds is closer to the Inward-facing state.

Between residues 410-440, the Apo systems are more likely to form a small 3-10 he-lix structure (residues 431-435) at the connection between two alpha helices between residues 410-440. In contrast, Ben, La, and Koa maintain an alpha-helical structure throughout residues 431-440, suggesting differing structural stability in this region compared to the Apo systems. Residues 410-440 are located near the ECD. Compound binding may stabilize the alpha-helix structure, potentially making the overall structure more compact and preventing compounds and urate ions from entering or exiting through the ECD.

### 3.9 Key residues analysis

Figure 10 shows the top 10 residues that contribute most to the binding free energy in the Ben, La, and Koa systems. Table S3 shows the alanine scanning results for representative conformations of the three systems, which support and complement the identification of key residues. The key

**Table 5.** Caver analysis data.

| System | State | Avg. Bottleneck Radius (Å) | Avg. Tunnel Length (Å) | Avg. Tunnel Curvature (Å) | Avg. Tunnel Throughput |
|---|---|---|---|---|---|
| **Apo** | 1 | 1.783 | 19.144 | 1.442 | 0.72280 |
| | 2 | 1.465 | 26.824 | 1.194 | 0.54864 |
| **Ben** | 1 | 2.037 | 24.008 | 1.280 | 0.72624 |
| | 2 | 2.191 | 19.188 | 1.136 | 0.78606 |
| **La** | 1 | 2.330 | 26.626 | 1.381 | 0.74755 |
| **Koa** | 1 | 2.088 | 20.890 | 1.286 | 0.74917 |
| | 2 | 2.474 | 13.599 | 1.097 | 0.84925 |

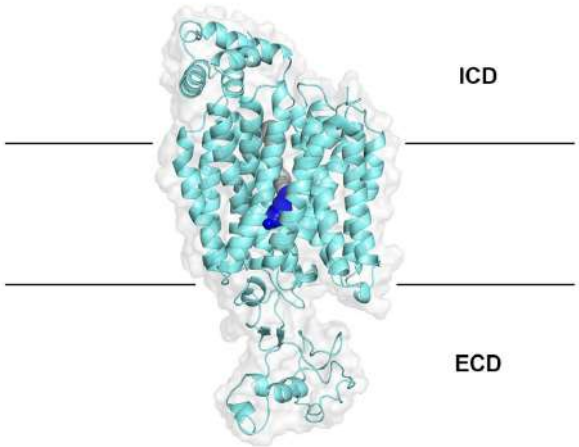


**Figure 8.** Channel analysis of State 2 in the Apo system. Gray represents channels facing the ICD, while blue represents those facing the ECD.

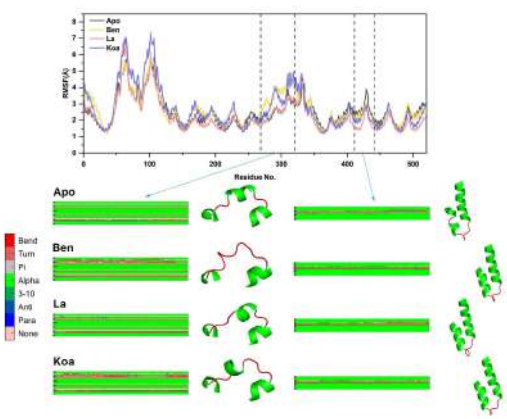


**Figure 9.** Top 10 key residues of (A)Ben, (B)La, and (C)Koa system.

residues for Koa show significant overlap with those for Ben. Notably, residues such as Leu31, Met214, Phe241, Phe360, and Phe365 contribute substantially to the binding interactions in both systems. The binding mode of Koa also shares similarities with that of La. For instance, Arg477 and Met214 play a crucial role in the binding interactions in both systems. This suggests that Koa and Ben may share a similar binding mode with URAT1, while La exhibits a different binding mechanism.

To explore how key residues contribute to binding, we analyzed the frequency of hydrogen bond formation between the three compounds and URAT1 residues during the MD simulations, considering only interactions that occurred in more than 20 frames. The results are summarized in Table S4. Additionally, representative conformations were analyzed to observe other interactions, as shown in Figure S4.

Throughout the simulation, in the Ben system, Gln473 formed a hydrogen bond with Ben in approximately 19likely to form Pi-Pi interactions with Ben. These Pi-Pi interactions are the primary contributors to the binding free energy between Ben and URAT1.

Similarly, in the La system, Arg477 formed a hydrogen bond with La in approximately 94 of the frames. According to the representative conformation, other residues primarily contribute through van der Waals interactions. Hydrogen bonds and van der Waals forces are the major contributors to the binding free energy between La and URAT1.

In the Koa system, Arg477 formed a hydrogen bond with Koa in approximately 72Phe365 are likely to engage in Pi-Alkyl interactions with Koa. Both hydrogen bonds and Pi-Alkyl interactions are the main contributors to the binding free energy between Koa and URAT1.

In the study on OAT1, Tongyi Dou et al. proposed that phenylalanine(Phe) and tryptophan(Trp) with benzene rings form the conserved aromatic cage for substrate/inhibitor binding [50]. Based on the analysis of key residues, we similarly hypothesize that Phe241, Phe449, Phe365, and Phe360 are the constituent residues of the conserved aromatic cage in URAT1.

### 3.10 Markov state models analysis

To further investigate the relative stable states of each system and the changes in the helices forming the channels within the simulations, we conducted a Markov state model analysis of the trajectories.

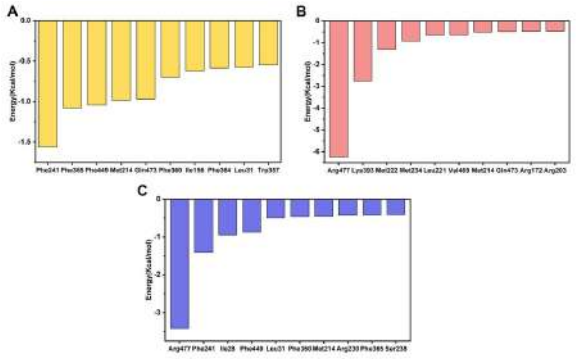

**Figure 10.** Top 10 key residues of (A)Ben, (B)La, and (C)Koa system.

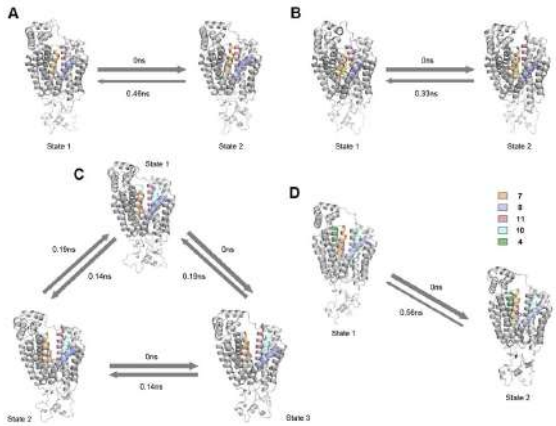

**Figure 11.** Transitions in Markov state models across the four systems. Highlighted in color are the helical regions near the channel with notable changes. (A)Apo. (B)Ben. (C)La. (D)Koa.

In the Apo system, as shown in Figure 11A, State 2 represents the stable state. Compared to State 1, helices 7 and 8 extend towards the ICD, while helix 11 moves closer to the channel center, and helix 7 moves away from the channel center. In the Ben system, as illustrated in Figure 11B, State 2 is the stable state. Compared to State 1, helices 7 and 11 extend towards the ICD, and helices 8 and 11 move away from the channel center. For the La system, as depicted in Figure 11C, State 3 is the stable state, State 1 is the unstable state, and State 2 is the intermediate state. During the transition from the unstable state to the stable state, helices 7 and 11 extend towards the ICD, and helices 7, 8, 10, and 11 move away from the channel center. In the Koa system, as shown in Figure 11D, State 2 represents the stable state. Compared to State 1, helices 4 and 7 shorten towards the ICD, and helices 7 and 8 move away from the channel center.

In summary, during the transition to a relatively stable state in the URAT1 system with compound binding, different helices forming the channel tend to move away from the channel center. This further confirms that binding of the compound induces URAT1 to adopt an inward-facing state.

## 4. Conclusion

In this study, we conducted a comprehensive investigation into the mechanisms of EOSR's anti-gout effects, including both direct and indirect mechanisms.

Network pharmacology explored the multi-target and multi-pathway actions of EOSR components on gout. PPI network analysis indicated that inflammatory targets, such as IL6, could be potential targets for EOSR in the treatment of acute gout attacks. Additionally, EOSR may influence uric acid excretion and reabsorption by targeting URAT1, among others. GO and KEGG enrichment pathway analyses demonstrated the regulation of inflammatory responses and multiple inflammation-related signaling pathways. EOSR may alleviate gout-induced inflammation and pain by inhibiting relevant targets and signaling pathways, thereby reducing the release of inflammatory mediators.

Through machine learning algorithms, molecular docking and MD simulation, we investigated the interactions between the important gout-related target URAT1 and two EOSR components (La and Koa). The results indicated that URAT1 undergoes a conformational change resembling an inward-facing state upon binding with the compounds. Concurrently, the secondary structure undergoes slight alterations. Certain regions of the ICD become more relaxed, while regions near the ECD become denser. These conformational changes in URAT1 may represent the molecular mechanism by which the compounds inhibit uric acid reabsorption, thereby exerting anti-gout effects. Additionally, the binding free energies of La and Koa to URAT1 are better than that of Ben. Koa shares similar key residues with Ben, and both Koa and La induce comparable conformational changes in URAT1. Based on the high similarity between these two components and Ben, we consider them potential inhibitors of URAT1.

To summarize, this study provides a comprehensive understanding of the pharmacological mechanisms and potential therapeutic impact of EOSR components in gout intervention. The identification of crucial components, targets, and signaling pathways holds promise for the development of novel treatments for gout. However, further experimental validation and clinical trials are imperative to confirm the efficacy and safety of EOSR, potentially paving the way for its utilization as a preventive and therapeutic agent for gout and associated conditions.

## Supporting Information

The following supporting information can be downloaded at: https://global-sci.com/storage/self-storage/cicc-2024-334-r1-si.pdf

Figure S1: Venn diagram showing 93 common targets between essential oils of sunflower receptacles (EOSR) and gout; Figure S2: The time-dependent variation of binding free energies between small molecules and URAT1; Figure S3: DSSP of the four system. (A) Apo (B) Ben (C) La (D); Koa Figure S4: Representative conformations from MD simulations. (A) Ben (B) Koa (C) La; Figure S5: Implied time scales of the four system. The lag time is black and an bracket indicates the independent ITS. (A) Apo (B) Ben (C) La (D) Koa; Figure S6: Implied timescales separation per index and timescale. (A) Apo (B) Ben (C) La (D) Koa; Figure S7: CK test of the four systems. (A) Apo (B) Ben (C) La (D) Koa; Table S1: 104 Compounds Information; Table S2: EOSR and gout targets, and their intersection; Table S3: Alanine scan results; Table S4: Hydrogen bond analysis.

## Acknowledgments

This research was funded by the Outstanding Young and Middle-aged Talent (Teams) for Scientific and Technological Innovation and Entrepreneurship in Jilin Province (20230508072RC), Natural Science Foundation of Jilin Province (YDZJ202301ZYTS121) and Key Project of the Jilin Education Department (JJKH20231140KJ).

## References

[1] Dalbeth N, Choi H K, Joosten L A B, Khanna P P, Matsuo H, Perez-Ruiz F, and Stamp L K, Gout, *Nat. Rev. Dis. Primers.*, **5** (2019), 69.

[2] Barnett R, Gout, *Lancet.*, **391** (2018), 2595.

[3] McCormick N, Yokose C, Challener G J, Joshi A D, Tanikella S, and Choi H K, Serum urate and recurrent gout, *JAMA.*, **331** (2024), 417–424.

[4] Wyngaarden J B, Overproduction of uric acid as the cause of hyperuricemia in primary gout, *J. Clin. Invest.*, **36** (1957), 1508–1515.

[5] Tan P K, Farrar J E, Gaucher E A, and Miner J N, Coevolution of URAT1 and uricase during primate evolution: Implications for serum urate homeostasis and gout, *Mol. Biol. Evol.*, **33** (2016), 2193–2200.

[6] Cochrane D J, Jarvis B, and Keating G M, Etoricoxib, *Drugs.*, **62** (2002), 2637–2651.

[7] Roberts W N, Liang M H, and Stern S H, Colchicine in acute gout: Reassessment of risks and benefits, *JAMA.*, **257** (1987), 1920–1922.

[8] van Durme C M P G, Wechalekar M D, and Landewé R B M, Nonsteroidal anti-inflammatory drugs for treatment of acute gout, *JAMA.*, **313** (2015), 2276–2277.

[9] Tayar J H, Lopez-Olivo M A, and Suarez-Almazor M E, Febuxostat for treating chronic gout, *Cochrane Database Syst. Rev.*, **11** (2012), CD008653.

[10] Heel R C, Brogden R N, Speight T M, and Avery G S, Benzbromarone: A review of its pharmacological properties and therapeutic use in gout and hyperuricaemia, *Drugs.*, **14** (1977), 349–366.

[11] Ogryzlo M A, Urowitz M B, Weber H M, and Houpt J B, The treatment of gout and disorders of uric acid metabolism with allopurinol, *Can. Med. Assoc. J.*, **95** (1966), 1120–1127.

[12] Hoy S M, Lesinurad: First global approval, *Drugs.*, **76** (2016), 509–516.

[13] Shi X, Zhao T, da Silva-Júnior E F, Zhang J, Xu S, Gao S, Liu X, and Zhan P, Novel urate transporter 1 (URAT1) inhibitors: A review of recent patent literature (2020–Present), *Expert Opin. Ther. Pat.*, **32** (2022), 1175–1184.

[14] Terkeltaub R, Emerging urate-lowering drugs and pharmacologic treatment strategies for gout: A narrative review, *Drugs.*, **83** (2023), 1501–1521.

[15] Zeng X, Liu Y, Fan Y, Wu D, Meng Y, and Qin M, Agents for the treatment of gout: Current advances and future perspectives, *J. Med. Chem.*, **66** (2023), 14474–1493.

[16] Shawon S I, Reyda R N, and Qais N, Medicinal herbs and their metabolites with biological potential to protect and combat liver toxicity and its disorders: A review, *Heliyon.*, **10** (2024), e25340.

[17] Lopes D C D X P, de Oliveira T B, Viçosa A L, Valverde S S, and Ricci Júnior E, Anti-inflammatory activity of the Compositae family and its therapeutic potential, *Planta Med.*, **87** (2021), 71–100.

[18] Ulewicz-Magulska B and Wesolowski M, Antioxidant activity of medicinal herbs and spices from plants of the Lamiaceae, Apiaceae, and Asteraceae families: Chemometric interpretation of the data, *Antioxid.*, **12** (2023), 2039.

[19] Li L, Teng M, Liu Y, Qu Y, Zhang Y, Lin F, and Wang D, Anti-gouty arthritis and antihyperuricemia effects of sunflower (Helianthus annuus) head extract in gouty and hyperuricemia animal models, *BioMed Res. Int.*, 2017, Article ID 5852076.

[20] He Y, Liu K, Han L, and Han W, Clustering analysis, structure fingerprint analysis, and quantum chemical calculations of compounds from essential oils of sunflower (Helianthus annuus L.) receptacles, *Int. J. Mol. Sci.*, **23** (2022), 10169.

[21] Liu L, Jiao Y, Yang M, Wu L, Long G, and Hu W, Network pharmacology, molecular docking and molecular dynamics to explore the potential immunomodulatory mechanisms of deer antler, *Int. J. Mol. Sci.*, **24** (2023), 10370.

[22] Bai X, Zhao X, Liu K, Yang X, He Q, Gao Y, Li W, and Han W, Mulberry leaf compounds and gut microbiota in Alzheimer's disease and diabetes: A study using network pharmacology, molecular dynamics simulation, and cellular assays, *Int. J. Mol. Sci.*, **25** (2024), 4062.

[23] Zou F, Li X, Yang R, Zhang R, and Zhao X, Effects and underlying mechanisms of food polyphenols in treating gouty arthritis: A review on nutritional intake and joint health, *J. Food Biochem.*, **46** (2022), e14072.

[24] Piñero J, Ramírez-Anguita J M, Saüch-Pitarch J, Ronzano F, Centeno E, Sanz F, and Furlong L I, The DisGeNET knowledge platform for disease genomics: 2019 update, *Nucleic Acids Res.*, **48** (2020), D845–D855.

[25] Stelzer G, Rosen N, Plaschkes I, Zimmerman S, Twik M, Fishilevich S, Stein T I, Nudel R, Lieder I, Mazor Y, Kaplan S, Dahary D, Warshawsky D, Guan-Golan Y, Kohn A, Rappaport N, Safran M, and Lancet D, The GeneCards suite: From gene data mining to disease genome sequence analyses, *Curr. Protoc. Bioinforma.*, **54** (2016), 1.30.1–1.30.33.

[26] Whirl-Carrillo M, Huddart R, Gong L, Sangkuhl K, Thorn C F, Whaley R, and Klein T E, An evidence-based framework for evaluating pharmacogenomics knowledge for personalized medicine, *Clin. Pharmacol. Ther.*, **110** (2021), 563–572.

[27] Daina A, Michielin O, and Zoete V, SwissTargetPrediction: Updated data and new features for efficient prediction of protein targets of small molecules, *Nucleic Acids Res.*, **47** (2019), W357–W364.

[28] Bardou P, Mariette J, Escudié F, Djemiel C, and Klopp C, Jvenn: An interactive Venn diagram viewer, *BMC Bioinformatics.*, **15** (2014), 293.

[29] Szklarczyk D, Gable A L, Lyon D, Junge A, Wyder S, Huerta-Cepas J, Simonovic M, Doncheva N T, Morris J H, Bork P, Jensen L J, and von Mering C, STRING v11: Protein-protein association networks with increased coverage, supporting functional discovery in genome-wide experimental datasets, *Nucleic Acids Res.*, **47** (2019), D607–D613.

[30] Shannon P, Markiel A, Ozier O, Baliga N S, Wang J T, Ramage D, Amin N, Schwikowski B, and Ideker T, Cytoscape: A software environment for integrated models of biomolecular interaction networks, *Genome Res.*, **13** (2003), 2498–2504.

[31] Chen Y, Zhao Z, Li Y, Yang Y, Li L, Jiang Y, Lin C, Cao Y, Zhou P, Tian Y, Wu T, and Pang J, Baicalein alleviates hyperuricemia by promoting uric acid excretion and inhibiting xanthine oxidase, *Phytomedicine.*, **80** (2021), 153374.

[32] Seeliger D and de Groot B L, Ligand docking and binding site analysis with PyMOL and AutoDock/Vina, *J. Comput. Aided Mol. Des.*, **24** (2010), 417–422.

[33] Singh R, Sledzieski S, Bryson B, Cowen L, and Berger B, Contrastive learning in protein language space predicts interactions between drugs and protein targets, *Proc. Natl. Acad. Sci. U. S. A.*, **120** (2023), e2220778120.

[34] Mysinger M M, Carchia M, Irwin J J, and Shoichet B K, Directory of useful decoys, enhanced (DUD-E): Better ligands and decoys for better benchmarking, *J. Med. Chem.*, **55** (2012), 6582–6594.

[35] Lomize M A, Pogozheva I D, Joo H, Mosberg H I, and Lomize A L, OPM database and PPM web server: Resources for positioning of proteins in membranes, *Nucleic Acids Res.*, **40** (2012),

D370–D376.

[36] Maier J A, Martinez C, Kasavajhala K, Wickstrom L, Hauser K E, and Simmerling C, ff14SB: Improving the accuracy of protein side chain and backbone parameters from ff99SB, *J. Chem. Theory Comput.*, **11** (2015), 3696–3713.

[37] Jamsawang P, Comparison of simple potential functions for simulating liquid water, 2018.

[38] He X, Man V H, Yang W, Lee T-S, and Wang J, A fast and high-quality charge model for the next-generation general AMBER force field, *J. Chem. Phys.*, **153** (2020), 114502.

[39] Lee J, Hitzenberger M, Rieger M, Kern N R, Zacharias M, and Im W, CHARMM-GUI supports the Amber force fields, *J. Chem. Phys.*, **153** (2020), 035103.

[40] Davidchack R L, Handel R, and Tretyakov M V, Langevin thermostat for rigid body dynamics, *J. Chem. Phys.*, **130** (2009), 234101.

[41] Roe D R and Cheatham T E, PTRAJ and CPPTRAJ: Software for processing and analysis of molecular dynamics trajectory data, *J. Chem. Theory Comput.*, **9** (2013), 3084–3095.

[42] Scherer M K, Trendelkamp-Schroer B, Paul F, Pérez-Hernández G, Hoffmann M, Plattner N, Wehmeyer C, Prinz J-H, and Noé F, PyEMMA 2: A software package for estimation, validation, and analysis of Markov models, *J. Chem. Theory Comput.*, **11** (2015), 5525–5542.

[43] Michaud-Agrawal N, Denning E J, Woolf T B, and Beckstein O, MDAnalysis: A toolkit for the analysis of molecular dynamics simulations, *J. Comput. Chem.*, **32** (2011), 2319–2327.

[44] Granados J C, Bhatnagar V, and Nigam S K, Blockade of organic anion transport in humans after treatment with the drug probenecid leads to major metabolic alterations in plasma and urine, *Clin. Pharmacol. Ther.*, **112** (2022), 653–664.

[45] Eckenstaler R and Benndorf R A, The role of ABCG2 in the pathogenesis of primary hyperuricemia and gout—An update, *Int. J. Mol. Sci.*, **22** (2021), 6678.

[46] Sharon Y and Schlesinger N, Beyond joints: A review of ocular abnormalities in gout and hyperuricemia, *Curr. Rheumatol. Rep.*, **18** (2016), 37.

[47] Stamp L K and Dalbeth N, Prevention and treatment of gout, *Nat. Rev. Rheumatol.*, **15** (2019), 68–70.

[48] The Gene Ontology Consortium, The Gene Ontology resource: Enriching a gold mine, *Nucleic Acids Res.*, **49** (2021), D325–D334.

[49] Saito H, Toyoda Y, Takada T, Hirata H, Ota-Kontani A, Miyata H, Kobayashi N, Tsuchiya Y, and Suzuki H, Omega-3 polyunsaturated fatty acids inhibit the function of human URAT1, a renal urate re-absorber, *Nutrients.*, **12** (2020), 1601.

[50] Dou T, Lian T, Shu S, He Y, and Jiang J, The substrate and inhibitor binding mechanism of polyspecific transporter OAT1 revealed by high-resolution cryo-EM, *Nat. Struct. Mol. Biol.*, **30** (2023), 1794–1805.

[51] Brezovsky J, Kozlikova B, and Damborsky J, Computational analysis of protein tunnels and channels, *Methods Mol. Biol.*, **1685** (2018), 25–42.

[52] Shen Z, Xu L, Wu T, Wang H, Wang Q, Ge X, Kong F, Huang G, and Pan X, Structural basis for urate recognition and apigenin inhibition of human GLUT9, *Nat. Commun.*, **15** (2024), 5039.